EPJ Web of Conferences **356**, 01024 (2026) https://doi.org/10.1051/epjconf/202635601024
ICC 2025

Study of structural, electronic, & thermoelectric properties of half-heusler alloy ZrSiPt: A first principles study

Shivani Thakur[1*], *Santu Baidya*[1]

[1]Department of Physics and Materials Science, Jaypee University of Information Technology, Waknaghat, Solan, Himachal Pradesh, India 173234

Abstract: In this work, we have studied the structural, electronic, and thermoelectric properties of the half-Heusler compound ZrSiPt using first-principles density functional theory calculations. Our calculations show that ZrSiPt is a semiconductor with a small band gap. Its electronic states near the Fermi level are mainly contributed by Zr-d and Pt-d orbitals. Phonon dispersion confirms that the compound is mechanically and dynamically stable, as indicated by the absence of imaginary phonon modes. Boltzmann transport calculations within the constant relaxation time approximation show the highest Seebeck coefficient of 1569 μV/K at 300 K. The highest electrical conductivity per relaxation time is 5.048×10^{20} S m^{-1} s^{-1} at 300 K. Further, the highest power factor reaches 1.14×10^{12} W m^{-1} K^{-2} s^{-1} at 300 K, indicating promising thermoelectric performance. Our results show that moderate tuning in ZrSiPt will enhance the thermoelectric performance, which is beneficial for future thermoelectric applications.

1 Introduction

Thermoelectric materials, which can directly convert heat into electrical energy and vice versa, have attracted considerable attention due to their potential for waste heat management and solid-state cooling applications. The efficiency of a thermoelectric material is commonly evaluated using the dimensionless figure of merit, defined as $ZT = \frac{S^2\sigma T}{\kappa}$, where $'S'$ denotes the Seebeck coefficient, $'\sigma\ '$ the electrical conductivity, $'\kappa'$ the total thermal conductivity, and $'T'$ the absolute temperature [1-4]. A high thermoelectric figure of merit can only be obtained when a strong Seebeck coefficient and efficient electrical transport are achieved. In this respect, half-heusler compounds are of particular interest, as they combine excellent thermal and mechanical stability with electronic characteristics that can be effectively tailored through compositional control. These intermetallic compounds, with the general formula *XYZ*, typically exhibit narrow band gaps and high Seebeck coefficients, which are favourable for thermoelectric energy conversion. Among different thermoelectric materials, half-Heusler compounds have attracted significant attention due to their excellent thermoelectric performance at high temperatures, thermal stability, mechanical robustness, and low toxicity

* Corresponding author: shivaniisthakur52@gmail.com

[5,6]. In recent years, Zr-based half-heusler alloys have gained interest due to their excellent thermoelectric performance. Ai *et. al*. reported that ZrNiSn-based half-heusler thermoelectrics can be fabricated using reactive sintering benefit from microstructural hierarchy, resulting in reduced lattice thermal conductivity while retaining efficient carrier transport. The optimised ZrHfNiSSb alloy achieved an enhanced ZT = 1.33 at 873 K [7]. Ranjan *et. al*. theoretically predicted that entropy-stabilised mixed half-heusler alloys such as ZrHfCoNiSnSb exhibit an enhanced thermoelectric performance, with a predicted ZT ≈ 1.0 at 1100 K [8]. Issaad *et. al.* studied Li-based half-Heusler alloys using first-principles density functional theory to analyse their electronic, elastic, magnetic, and thermoelectric properties. They reported that LiCrSi and LiCrP are stable compounds with half-metallic behaviour and show promising thermoelectric performance [9]. Shastri *et. al.* studied Fe_2ScX (X = P, As, Sb) full-Heusler compounds using DFT and found a suitable band gaps and promising thermoelectric performance at high temperatures [10]. Vaitesswar *et. al.* carried out a machine-learning-based study to identify promising thermoelectric materials; however, a detailed understanding of the underlying structural, electronic, and thermoelectric properties remains limited [11]. In this study, we have reported the detailed structural, electronic and thermoelectric properties of ZrSiPt using first principles density functional theory.

2 Computational Details

The electronic structure calculations were conducted using density functional theory as implemented in the QUANTUM ESPRESSO package [12]. Exchange–correlation effects were incorporated using the Perdew–Burke–Ernzerhof (PBE) parametrisation within the generalised gradient approximation [13,14]. A plane-wave basis set with a cutoff energy of 35 Ry was used, and the Brillouin zone was sampled on an 8 × 8 × 8 Monkhorst–Pack mesh. Convergence of the total energy was ensured by imposing a threshold of 10^{-4} Ry. Transport and thermoelectric properties were then obtained by applying the semiclassical Boltzmann transport formalism under the constant relaxation-time approximation, employing the BoltzTrap code [15].

3 Structural Properties

Figure 1 shows the crystal structure of bulk ZrSiPt optimised using DFT calculations. ZrSiPt is a half-heuslar alloy crystallised in the cubic F-43m space group. Table 1 shows the optimised lattice constant and atomic positions with Wyckoff positions of bulk ZrSiPt.

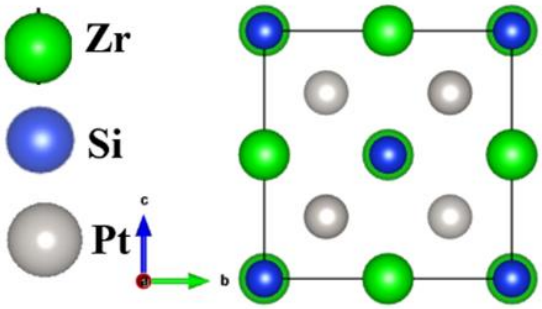

Fig. 1. Crystal structure of ZrSiPt

The calculated lattice constants are optimised using first-principles calculations as implemented in Quantum Espresso.

Table 1 optimised lattice constant and atomic positions with Wyckoff positions of bulk ZrSiPt. Optimised lattice constant: $a = b = c = 6.03$ Å

Atom	*x*	*y*	*z*	Wyckoff Position
Si	0.000	0.000	0.000	4a
Zr	0.500	0.000	0.000	4b
Pt	0.250	0.250	0.750	4d

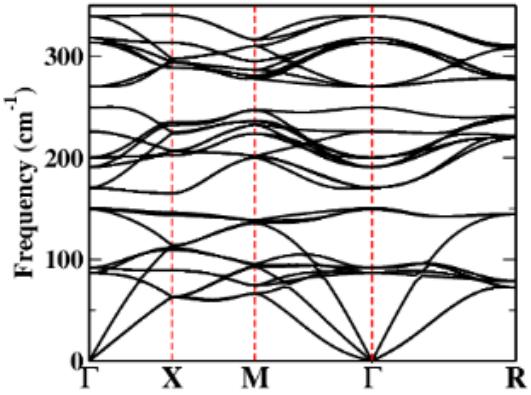

Fig. 2. Phonon dispersion spectra of ZrSiPt

The phonon dispersion of ZrSiPt is presented in Figure 2. The absence of imaginary phonon modes throughout the Brillouin zone indicates the dynamical stability of the system, validating the robustness of the optimised crystal structure.

4 Electronic Properties

Figure 3 presents the calculated electronic band structure together with the corresponding density of states, which provides clear insight into the electronic nature of bulk ZrSiPt.

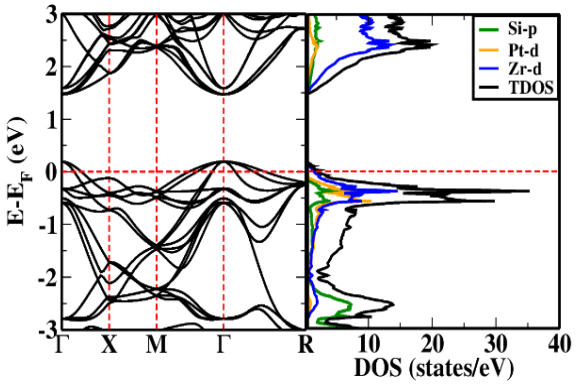

Fig. 3. Electronic band structure along with the density of states (DOS) of bulk ZrSiPt

The band dispersion reveals semiconducting behaviour characterised by an indirect band gap of approximately 1.06 eV located near the Fermi level, indicating that the valence band maximum and conduction band minimum occur at different high-symmetry points in the Brillouin zone. Further understanding of the electronic states is obtained from the orbital-projected density of states, which shows that the valence band region close to the Fermi energy is predominantly contributed by Pt-d and Si-p orbitals. In contrast, the conduction band is mainly composed of Zr-d orbitals, suggesting that zirconium plays a crucial role in the total density of states. This orbital contribution between the valence band and conduction band influences the electronic and thermoelectric properties of ZrSiPt.

5 Thermoelectric Properties

Figure 4 presents the calculated thermoelectric transport parameters of bulk ZrSiPt as functions of the chemical potential at temperatures of 300 K, 500 K, and 700 K. The variation of the Seebeck coefficient with chemical potential at different temperatures is shown in Figure 4(a). At 300 K, the Seebeck coefficient reaches a maximum value of 1569.2 μV K^{-1}. With an increase in temperature to 500 K, this maximum value decreases slightly to 1556.6 μV K^{-1}, and a further reduction to 1550.7 μV K^{-1} is observed at 700 K.

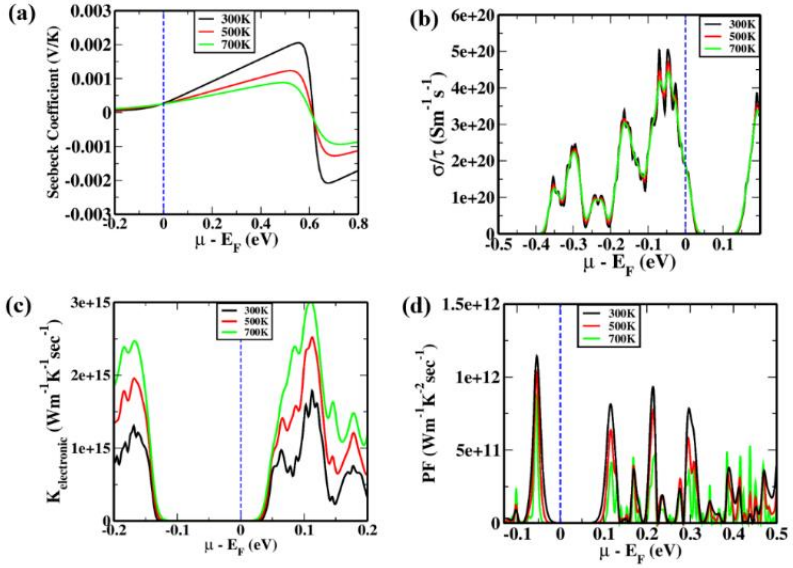

Fig. 4: Thermoelectric properties as a function of chemical potential at 300K, 500K and 700K (a) Seebeck coefficient (b) Electrical conductivity per unit relaxation time (σ/τ) (c) Electronic thermal conductivity per unit relaxation time (κ_e/τ) (d) Power factor per unit relaxation time ($S^2\sigma/\tau$).

This gradual decline in the Seebeck coefficient with the elevation of temperature can be attributed to enhanced thermal excitation of charge carriers, which leads to a more symmetric distribution of electrons and holes around the chemical potential. As a result, the net asymmetry in carrier transport responsible for generating thermoelectric voltage is reduced, yielding lower Seebeck values at elevated temperatures [16].

The dependence of electrical conductivity per unit relaxation time on chemical potential is illustrated in Figure 4(b) at 300 K, 500 K and 700 K. The maximum electrical conductivity is obtained at 300 K, with a value of 5.048×10^{20} S $m^{-1}s^{-1}$. Upon increasing the temperature

to 500 K, the conductivity decreases to 4.7×10^{20} S $m^{-1}s^{-1}$, followed by a further reduction to 4.44×10^{20} S $m^{-1}s^{-1}$ at 700 K. This temperature-induced decrease in electrical conductivity is primarily associated with stronger electron–phonon interactions at higher temperatures, where lattice vibrations reduce carrier mobility and consequently suppress the charge transport [17]. Figure 4(c) presents the electronic contribution to thermal conductivity per unit relaxation time as a function of chemical potential at 300 K, 500 K and 700 K. The lowest electronic thermal conductivity is observed at room temperature, with a value of 2.48×10^9 W m^{-1} K^{-1} s^{-1}. As the temperature increases to 500 K, this value rises to 3.104×10^9 W m^{-1} K^{-1} s^{-1}, and a pronounced increase to 1.55×10^{10} W m^{-1} K^{-1} s^{-1} is obtained at 700 K. The comparatively low electronic thermal conductivity at 300 K suggests reduced heat transport by charge carriers, which is favourable for thermoelectric performance.

The calculated power factor per unit relaxation time is shown in Figure 4(d). The maximum power factor is found at 300 K with a value of 1.143×10^{12} W m^{-1} K^{-2} s^{-1}. As the temperature increases to 500 K, the peak power factor decreases to 1.038×10^{12} W m^{-1} K^{-2} s^{-1}, and a further reduction to 8.86×10^{11} W m^{-1} K^{-2} s^{-1} is observed at 700 K. The overall decrease in power factor with temperature reflects the combined influence of reduced Seebeck coefficient and declining electrical conductivity at elevated temperatures.

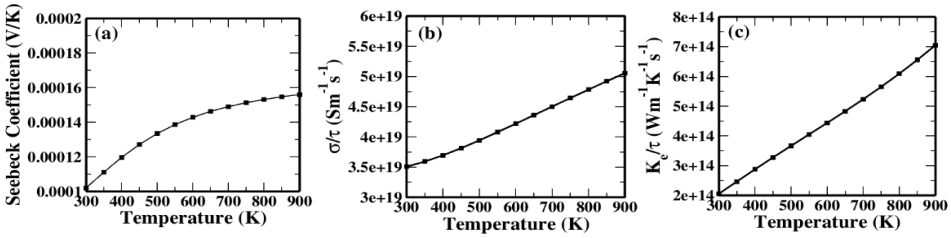

Fig. 5. Thermoelectric properties as a function of temperature at Fermi level (a) Seebeck coefficient (b) Electrical conductivity per unit relaxation time (σ/τ) (c) Electronic thermal conductivity per unit relaxation time (κ_e/τ).

Figure 5 shows the variation of thermoelectric properties with temperature. Figure 5(a) shows that the Seebeck coefficient increases continuously with increasing temperature. Figure 5(b) shows that the electrical conductivity per unit relaxation time also increases with temperature at the fermi level due to the increase in thermally excited charge carriers. Figure 5(c) shows that the electronic thermal conductivity per unit relaxation time increases steadily as the temperature increases.

6 Summary and Conclusions

In conclusion, first-principles calculations were employed to systematically investigate the structural, electronic, and thermoelectric characteristics of the half-Heusler compound ZrSiPt. Phonon dispersion confirms that ZrSiPt is both mechanically and thermally stable. It is a narrow-gap semiconductor, with Zr-d and Pt-d orbitals dominating near the Fermi level. Boltzmann transport calculations show a highest Seebeck coefficient of 1569 μV/K, electrical conductivity per unit relaxation time of 5.048×10^{20} S m^{-1} s^{-1}, and a power factor of 1.14×10^{12} W m^{-1} K^{-2} s^{-1} at 300 K, indicating good thermoelectric performance and shows the applications for room temperature thermoelectric devices.

References

1. Abderrazak Boutramine, S. Al-Qaisi, N. Sfina, L. Ait Lamine, H. Chaib, M. Archi, O. Alsalmi, and S. Rabhi, *Insights into the thermodynamic, optoelectronic, and thermoelectric properties of ternary transition metal chalcogenides BiIrQ (Q = S, Se, Te) for next-generation optoelectronic and energy harvesting technologies: A DFT and AIMD study*. **Surfaces and Interfaces 72**, 107269 (2025). https://doi.org/10.1016/j.surfin.2025.107269.
2. W. Li, S. Ghosh, N. Liu, B. Poudel, Half-Heusler thermoelectrics: Advances from materials fundamental to device engineering. *J. Joule* **8**, 1274–1311 (2024). https://doi.org/10.1016/j.joule.2024.03.016.
3. D. P. Rai, A. Shankar, Sandeep, M. P. Ghimire, R. Khenata, and R. K. Thapa, *Study of the enhanced electronic and thermoelectric (TE) properties of $Zr_xHf_{1-x-y}Ta_yNiSn$: A first principles study*. **RSC Advances 5**, 95353–95359 (2015). https://doi.org/10.1039/C5RA12897H.
4. R. K. Giri, M. B. Solanki, S. H. Chaki, and M. P. Deshpande, *The DFT study of thermoelectric properties of $CuInS_2$: A first principle approach*. **IOP Conf. Ser.: Mater. Sci. Eng. 1291**, 012009 (2023). https://doi.org/10.1088/1757-899X/1291/1/012009.
5. G. Alghamdi and R. Kumar, *Thermoelectric properties of Pr_3Se_4 compound: DFT study*. **ECS Transactions 107**, 12265 (2022). https://doi.org/10.1149/10701.12265ecst.
6. T. Graf, C. Felser, S. S. P. Parkin, Simple rules for the understanding of Heusler compounds. *Prog. Solid State Chem.* **39**, 1–50 (2011).
7. Ai, X., Wu, Y., Lyu, H., et al. (2025). High-performance ZrNiSn-based half-Heusler thermoelectrics with hierarchical architectures enabled by reactive sintering. *Nature Communications, 16*, 6497. https://doi.org/10.1038/s41467-025-61868-x.
8. R. Ranjan, Entropy-stabilized ZrHfCoNiSnSb half-Heusler alloy for thermoelectric applications: a theoretical prediction. *Phys. Chem. Chem. Phys.* **27**, 15622–15634 (2025). https://doi.org/10.1039/D5CP01601K.
9. F. Issaad, A. Maafa, H. Rozale, M. A. Boukli Hacene, and A. Bouabça, Electronic and thermoelectric properties of Li-based half-Heusler alloys: A DFT study. *Annals of West University of Timisoara – Physics* **62**, 95–107 (2020). https://doi.org/10.2478/awutp-2020-0006.
10. Shivprasad S. Shastri and Sudhir K. Pandey, Two functionals approach in DFT for the prediction of thermoelectric properties of Fe_2ScX (X = P, As, Sb) full-Heusler compounds. *J. Phys.: Condens. Matter* **31**, 435701 (2019). https://doi.org/10.1088/1361-648X/ab2dd5.
11. U. S. Vaitesswar, D. Bash, T. Huang, J. Recatala-Gomez, T. Deng, S.-W. Yang, X. Wang, and K. Hippalgaonkar, Machine learning based feature engineering for thermoelectric ma terials by design. *Digital Discovery* **3**, 210–220 (2024). https://doi.org/10.1039/D3DD00131H.
12. P. Giannozzi *et al.*, *QUANTUM ESPRESSO: A modular and open-source software project for quantum simulations of materials*. **J. Phys.: Condens. Matter 21**, 395502 (2009). https://doi.org/10.1088/0953-8984/21/39/395502.
13. G. K. H. Madsen, *Functional form of the generalized gradient approximation for exchange: The PBEα functional*. **Phys. Rev. B 75**, 195108 (2007). https://doi.org/10.1103/PhysRevB.75.195108.

14. J. P. Perdew, K. Burke, and M. Ernzerhof, *Generalised gradient approximation made simple*. **Phys. Rev. Lett. 77**, 3865–3868 (1996). https://doi.org/10.1103/PhysRevLett.77.3865.
15. G. K. H. Madsen and D. J. Singh, *BoltzTraP: A code for calculating band-structure dependent quantities*. **Comput. Phys. Commun. 175**, 67–71 (2006). https://doi.org/10.1016/j.cpc.2006.03.007.
16. F. Shirvani, Z. Razavifar, *Exploration of structural, electrical, and thermoelectric properties of two-dimensional WTe_2 in three phases through ab initio investigations*, **PhysicaB: Condens. Matter 696**, 416609 (2025). https://doi.org/10.1016/j.physb.2024.416609.
17. S. S. Nair, N. Singh, *Mechanisms and design principles for optimizing lattice thermal conductivity in chalcogenides: A comprehensive review*, **Materials Today Physics 57**, 101785 (2025). https://doi.org/10.1016/j.mtphys.2025.101785.